

Role of the Propionic Acid Side-Chain of C-Phycocyanin Chromophores in the Excited States for the Photosynthesis Process

Kenji Mishima, Mitsuo Shoji, Yasufumi Umena, Mauro Boero, Yasuteru Shigeta

▶ **To cite this version:**

Kenji Mishima, Mitsuo Shoji, Yasufumi Umena, Mauro Boero, Yasuteru Shigeta. Role of the Propionic Acid Side-Chain of C-Phycocyanin Chromophores in the Excited States for the Photosynthesis Process. Bulletin of the Chemical Society of Japan, 2020, 93 (12), pp.1509-1519. 10.1246/bcsj.20200187 . hal-02990698

HAL Id: hal-02990698
https://hal.science/hal-02990698

Submitted on 3 Jun 2021

HAL is a multi-disciplinary open access archive for the deposit and dissemination of scientific research documents, whether they are published or not. The documents may come from teaching and research institutions in France or abroad, or from public or private research centers.

L'archive ouverte pluridisciplinaire **HAL**, est destinée au dépôt et à la diffusion de documents scientifiques de niveau recherche, publiés ou non, émanant des établissements d'enseignement et de recherche français ou étrangers, des laboratoires publics ou privés.

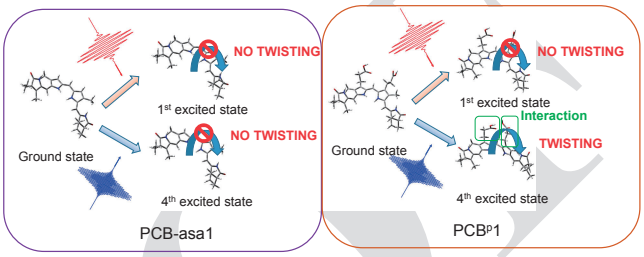
BULLETIN
OF THE
CHEMICAL SOCIETY OF JAPAN

Role of the Propionic Acid Side-Chain of C-Phycocyanin Chromophores in the Excited States for the Photosynthesis Process

Kenji Mishima,* Mitsuo Shoji,* Yasufumi Umena, Mauro Boero, and Yasuteru Shigeta

Bull. Chem. Soc. Jpn.
1–11

The present quantum chemistry calculations are aimed at unraveling the key role played by the C-phycocyanin (C-PC) chromophores, phycocyanobilin (PCB), in the light absorption and transmission in natural photosynthesis. The intramolecular interactions of propionic acid side-chains are crucial in determining the molecular geometries and photophysical properties in their excited states.



PROOF

BCSJ

Document type: Article

Role of the Propionic Acid Side-Chain of C-Phycocyanin Chromophores in the Excited States for the Photosynthesis Process

Kenji Mishima,*[1] Mitsuo Shoji,*[1,2] Yasufumi Umena,[3] Mauro Boero,[4] and Yasuteru Shigeta[1]

[1]Center for Computational Sciences, University of Tsukuba, 1-1-1 Tennodai, Tsukuba, Ibaraki 305-8577, Japan

[2]JST-PRESTO, 4-1-8 Honcho, Kawaguchi, Saitama 332-0012, Japan

[3]Department of Physiology, Division of Biophysics, Jichi Medical University, 3311-1 Yakushiji, Shimotsuke, Tochigi 329-0498, Japan

[4]University of Strasbourg, Institut de Physique et Chimie des Matériaux de Strasbourg, CNRS, UMR 7504, 23 rue du Loess, F-67034 France

E-mail: mishima.kenji.fu@u.tsukuba.ac.jp (K. Mishima), mshoji@ccs.tsukuba.ac.jp (M. Shoji)

Received: June 16, 2020; Accepted: August 10, 2020; Web Released: xxxxx xx, xxxx



Kenji Mishima
Kenji Mishima received his Ph.D. in applied chemistry from the University of Tokyo in 1999 under the supervision of Prof. Koichi Yamashita. Following postdoctoral work at Institute for Molecular Science (IMS) with Prof. Hiroki Nakamura (1999–2001), Institute of Atomic and Molecular Sciences (IAMS) in Taipei, Taiwan with Prof. Sheng Hsien Lin (2001–2004), and the University of Tokyo with Prof. Koichi Yamashita (2004–2019), he joined Center for Computational Sciences at University of Tsukuba as a postdoctoral associate in 2019. His current research interests are quantum chemistry calculations on solar cells and photosynthesis.



Mitsuo Shoji
Mitsuo Shoji received his Ph.D. in chemistry from Osaka University in 2007 under the supervision of Prof. Kizashi Yamaguchi. Following postdoctoral work at Nagoya University with Prof. Susumu Okazaki (2008–2010), he joined the Department of Physics at University of Tsukuba as an assistant professor in 2010 and moved to the present faculty in 2016. His current research interests are reaction mechanisms of enzyme reactions by utilizing QM/MM calculations and parallel computations.

Abstract

This paper focuses on a theoretical investigation of the peculiar properties of the chromophore in the C-phycocyanin (C-PC), phycocyanobilin (PCB). The scope is to unravel their key features upon light absorption and transmission occurring in natural photosynthesis. To this aim, by resorting to the time-dependent density functional theory (TDDFT) and natural bond orbital (NBO) methods, we compute the photoabsorption spectra and electronic properties of PCB, showing that three different orientations of the PCB in C-PC contribute to the nonhomogeneous broadening of the entire photoabsorption spectrum of C-PC. Furthermore, the photoabsorption peaks of PCB can undergo a shift up to 40 nm because of solvation effects. Further investigations on the competitive influence of the nearby aspartate residue and two propionic acids on the absorption spectra show that the latter play a significant role in realizing the different photo-response among the three isomers of PCB. In the low-lying electronic excited states, the π conjugated C-C bonds and the twisting angle of the pyrrole rings turn out to be affected. The NBO geometrical analyses of the bond lengths, interatomic angles, and dihedral angles evidenced that the intermolecular interactions of the propionic acid side chains play a crucial role in the determination of the excited state molecular conformations. These results indicate that the absorption spectra and the excited state structures of PCB are efficiently tuned during natural photosynthesis processes.

Keywords: C-Phycocyanin chromophore | Electronic excited states | Time-dependent density functional theory

1. Introduction

Pigment molecules play an essential role in the first stage of a wealth of photosynthesis processes involving light-harvesting, photoenergy transfer, and conversion of photons into electric

© 2021 The Chemical Society of Japan

energy. In this general scenario, phycobilisomes, commonly found in cyanobacteria and red algae,[1] are known to absorb sunlight and, subsequently, transfer this energy to chlorophyll *a* (Chl a). The thermophilic cyanobacterium, *Synechococcus elongates*, is one of the organisms exploiting a light-harvesting complex termed phycobilisome. In this cyanobacterium, the phycobilisome protein complex is composed of phycobiliproteins, allophycocyanin (A-PC), C-phycocyanin (C-PC), and linker proteins.[2] For instance, two subunits of C-PC, α and β,[3] covalently bind one (α-84) and two (β-84, and β-155) PCB pigments in phycobiliproteins from *Synechococcus elongates*.[4] All of these three PCBs have similar chemical structures composed of linear tetrapyrroles.[5] Despite these structural analogies, it has been shown that these PCBs have different photophysical properties.[6] This indicates that the light harvesting activity of C-PC is an intriguing process more complicated than what a simple analysis based solely on the structural inspection could suggest. It is then not surprising that several experimental and theoretical studies have been undertaken to understand structural, photophysical, and chemical properties of C-PC. The first seminal spectroscopic study was conducted for the C-PC trimer extracted from the thermophilic cyanobacterium *Mastigocladus laminosus*.[7] Absorption, circular dichroism, fluorescence, and fluorescence polarization spectroscopies were used to probe both the steady state and the pathway responsible for the energy transfer in the C-PC trimer.[7] After this milestone work, two research lines have become prominent in the study of the C-PC in photosynthesis mechanism: The first one focuses on photophysical properties, whereas the second one on structural properties.

On one hand, from a photophysical standpoint, a series of C-PC chromophores present a common feature. Namely, their absorption spectra consist of two main light-absorbing bands named Soret band and Q band. The former lies in the wavelength range between 350 and 450 nm while the latter, in the range between 450 and 700 nm.[8,9] The Soret band is important due to the characteristic features ascribed to the transition from the highest occupied molecular orbital (HOMO) to the lowest unoccupied one (LUMO).[10–12] To date, the photophysical properties of C-PC, and in particular, the absorption spectra, have been numerically simulated and compared to experimental results[7] to deduce the quantum chemical nature of the transitions involved.[10–17] To this aim, quantum chemistry (QC) calculations based on either density functional theory (DFT) or the time-dependent DFT (TDDFT) have been the preferred computational tools. The experimental results turned out to be satisfactorily reproduced at the B3LYP[18] level using a 6-31 G(d) localized basis set.

On the other hand, from a structural standpoint, identification of the crystal structures of C-PC at high resolution has been of fundamental importance not only to investigate the chromophores as a whole, but also to identify the intra-/inter-chromophore interactions, and to infer some plausible energy-transfer pathway. From these studies, it could be understood that phycobiliproteins of *Synechococcus elongates* are composed of α- and β-subunits. The α-subunit covalently binds one PCB chromophore at a cysteine residue α-84, whereas the β-subunit binds two PCBs at cysteine residues β-84 and β-155.[11] Combining this piece of information with that obtained from absorption and circular dichroism spectra, the energy transfer pathway was identified. In practice, the photon energy absorbed by β-84 is transferred to β-155,[11] and this agrees with the experimental wisdom.[7]

Recently, at variance with the investigations focused on the static molecular structure, time-resolved femtosecond dynamics of proteins undergoing photoabsorption has become an appealing investigation probe both experimentally and theoretically,[19,20] empowered by the rapid development of X-ray free-electron laser (XFEL).[21–23] For instance, femtosecond hard X-ray pulses available at the Linac Coherent Light Source allowed to identify the initial steps of the photoisomerization of a conjugated chromophore in photoactive yellow protein.[19] Moreover, experimental time-resolved serial femtosecond crystallography made possible by XFEL could resolve the ultrafast structural changes occurring in the carbonmonoxy myoglobin complex upon photolysis of the Fe-CO bond.[20] Complementary, hybrid quantum mechanics/molecular mechanics (QM/MM) simulations were used to get additional insights into the protein dynamics not accessible to experimental probes. In the same context, Coquelle and coworkers[24] performed picosecond time-resolved crystallography using XFEL, and were able to show that hydroxybenzylidene imidazolinone chromophore of rsEGFP2 in the excited state assumes a near-conical twisted configuration halfway between the *trans* and *cis* isomers. The experimental results turn out to be in line with excited-state QM/MM and classical molecular dynamics simulations.

Quantum chemical approaches were used by Durbeej[14] to investigate the molecular motion of the phytochromobilin (PΦB) chromophore induced by light absorption. To reduce the computational cost, Durbeej's model was based on the assumption that the thioether linkage at C3, the propionic carboxy groups of rings B and C at C8 and C12, the methyl groups at C2, C7, C13, and C17, and the ethyl groups at C3 and C18 were replaced by hydrogen atoms, as shown in Panel (a) of Figure 1. The calculations showed that the photoisomerization at C10 is favored with respect to those at C4 and at C15. On the other hand, Matute and coworkers[17] numerically investigated UV-vis absorption spectra of the photoreceptor chromophores biliverdin (BV) in the ZZZssa conformation and PCB with conformations ZZZssa and ZZZsas. Panel (b) of Figure 1 shows one of their model molecular structures: the PCB-asa model. However, both models lacked the two adjacent propionic acid groups, -CH_2-CH_2-COOH, attached directly to the pyrrole ring backbone in common as shown in Panel (c) of Figure 1, and their role, still unclear, is likely to be non-negligible.

The purpose of the present computational work is to shed some light on the role of two interacting adjacent propionic acid groups of PCB in the photoexcitation processes. To analyze the light-induced excitation of PCB, DFT-based optimizations are used to obtain the PCB in the ground state. Then, we resort to TDDFT to compute the excitation energies of low-lying excited states and the absorption spectrum of each PCB in C-PC. We provide evidence for the origin of the broadening of the experimental absorption spectra, ascribed here to the simultaneous presence of α-84, β-84, and β-155. The solvation effects on PCB were accounted for by the polarizable continuum models (PCMs). Natural bond orbital (NBO) analyses[25] were used to get a deeper insight into the different electronic properties of α-

© 2021 The Chemical Society of Japan

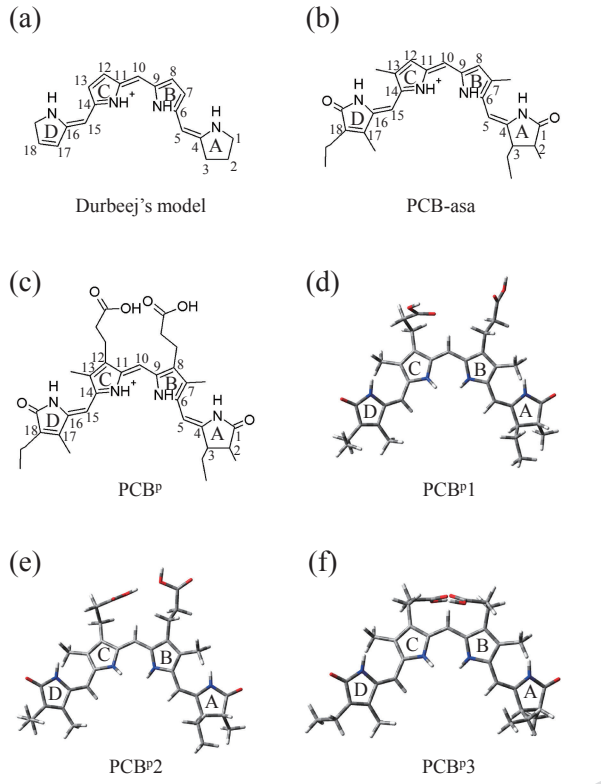


Figure 1. (a) Chemical structure of the Dubeej model.[14] (b) Chemical structure of the PCB-asa model of Matute and coworkers.[17] The main C atoms of the framework are numbered from 1 to 18. (c) PCB^{p} model with two propionic acid groups. Optimized molecular structures of (d) PCB^{p}1, (e) PCB^{p}2, and (f) PCB^{p}3 in the $\varepsilon = 4$ environment. The color code for atoms is white for H, gray for C, blue for N and red for O.

84, β-84, and β-155. Specifically, ionization potential, electron affinity, HOMO-LUMO gap, absolute electronegativity, hardness, global softness, dipole moment, isotropic polarizability, anisotropic polarizability, dielectric constant, molecular volume, and molecular electrostatic potential (MEP) were calculated and analyzed in detail since all of them, to various extents, are related to biologically relevant noncovalent interactions (e.g. van der Waals interactions of the molecule with its surrounding environment) as well as the individual characteristic features of PCB.

Finally, structural changes of PCB in the excited states are investigated including up to the 5th excited states. These structural changes are quantified in terms of the root mean square deviations (RMSDs), along with bond lengths, interatomic angles, and dihedral angles. From these analyses, the fundamental role of the two adjacent propionic acid groups of PCB in the excited states is assessed.

2. Theoretical Methods

All the QC calculations performed in this work were done with the Gaussian16 package.[26] Geometry optimizations for the ground states were done at the standard DFT level, while optimizations of the excited states, including up to the 5th state, were computed at the TDDFT level.[18,27] The B3LYP[18,28] functional was used to describe the exchange-correlation interaction and electronic wavefunctions were represented on a 6-31G(d) localized basis set were used without any symmetry restriction.

The initial structures of the chromophores in the α- and β–subunits of C-PC from *Synechococcus elongatus* were taken from the 1.45 Å resolution X-ray structure availabe in the Protein Data Bank (PDB ID: 1JBO).[29] The missing hydrogen atoms were added by means of GaussView, Version 6.1.[30] The C-PC from *Synechococcus elongatus* contains three different orientations of C-PCs, which are covalently bound via the cystein residues of either α-84, β-84, or β-155.

In the present study, we adopted two model structures: the PCB-asa model shown in Panel (b) of Figure 1 and the PCB^{p} model shown in Panel (c) of Figure 1. The superscript letter p in PCB^{p} denotes to the inclusion of the propionic acid side-chains to the theoretical model. The propionic acid side-chains at C8 and C12 are present in the PCB^{p} model. In the PCB-asa model, the propionic acid side-chains are truncated.

These models are composed of four pyrrole rings, labeled A, B, C, and D. In the open chain links, the outermost pyrrole rings are A and D, and each pyrrole ring contains one oxo atom, whereas oxo atoms are absent in the inner pyrrole rings B and C.

The PCB-asa and PCB^{p} models are used to elucidate the explict role of the two adjacent propionic acids. In the following, the C-PCs bound by the cystein redidues of α-84, β-84, or β-155 are referred to as PCB-asa1, PCB-asa2, and PCB-asa3 for the PCB-asa model, respectively, whereas those are referred to as PCB^{p}1, PCB^{p}2, and PCB^{p}3 for the PCB^{p} model, respectively. On the basis of former theoretical results on absorption and CD spectra[10,11] and potential energy surfaces,[15] singly protonated PCB-asa and PCB^{p} were assumed.

All the results for both the PCB-asa and PCB^{p} models are newly recalculated in the present study to complement unavailabe data.[17]

Using these structures as our starting configurations, geometry optimizations were performed. A dielectric constant of $\varepsilon = 4.0$ was used for the PCM[31] calculations to mimic the internal protein environment.[10–12,32] Hereafter, we shall refer to "the $\varepsilon = 4$ environment" to indicate this pseudo-protein environment. Similarly, $\varepsilon = 78.39$ was assumed for the water solvation. All the optimized molecular geometries were checked within the normal mode analysis to assess whether or not all the vibrational frequencies are positive.

The absorption spectra of fully optimized geometries in the ground state were calculated by TDDFT[18,27] with the same DFT parameters used for the geometry optimizations. The electronic vertical excitations were obtained using the same optimized structures in the gas phase or in the $\varepsilon = 4$ environment. We found that very similar absorption spectra, e.g., in the $\varepsilon = 4$ environment, were obtained even for molecular geometries initially in the gas phase, indicating that the resulting spectrum is rather insensitive to the pristine structural optimization. Therefore, molecular geometries obtained in the $\varepsilon = 4$ environment were used for all the absorption spectra in different solvents other than in the $\varepsilon = 4$ environment.

Using the computed light absorption wavelengths and the corresponding oscillator strengths, we fitted the absorption spectra by the superposition of Gaussian line shapes defined by

© 2021 The Chemical Society of Japan

$$I(\lambda) = I_{\max}\exp\left\{-\frac{4\ln 2}{FWHM^2}(\lambda - \lambda_{\max})^2\right\}, \quad (1)$$

where $I(\lambda)$ is the intensity of the absorption spectrum, $I_{\max}$ its maximum intensity, λ the wavelength, $\lambda_{\max}$ the wavelength at the maximum absorption intensity, and *FWHM* the full width at half maximum. *FWHM* was set to 30.0 nm in all the computational spectra presented in this study.

For the NBO analysis, the ionization potential (IP) and the electron affinity (EA) were calculated from the molecular orbital energies (ε_{HOMO} and ε_{LUMO}) as follows:[33]

$$IP = -\varepsilon_{HOMO}, \quad (2)$$

$$EA = -\varepsilon_{LUMO}. \quad (3)$$

The HOMO-LUMO gap (E_{GAP}), the absolute electronegativity (χ), and the hardness (η) were evaluated using the IE and EA:[34]

$$E_{GAP} = \varepsilon_{LUMO} - \varepsilon_{HOMO}, \quad (4)$$

$$\chi = \frac{IP + EA}{2}, \quad (5)$$

$$\eta = \frac{IP - EA}{2}. \quad (6)$$

The global softness (S) is defined as the inverse of the global hardness:[35]

$$S = \frac{1}{\eta}. \quad (7)$$

Apart from the dipole moment, an important molecular property is the polarizability tensor. Using the principal (diagonal) components,

$$\alpha_{xx}, \alpha_{yy}, \alpha_{zz}, \quad (8)$$

the isotropic polarizability, α_{iso}, can be written as:

$$\alpha_{iso} = (\alpha_{xx} + \alpha_{yy} + \alpha_{zz})/3. \quad (9)$$

The anisotropic polarizability, α_{aniso}, is then given by

$$\alpha_{aniso} = \sqrt{\frac{(\alpha_{xx} - \alpha_{yy})^2 + (\alpha_{xx} - \alpha_{zz})^2 + (\alpha_{yy} - \alpha_{zz})^2}{2}}. \quad (10)$$

The dielectric constant, ε, can be obtained by the "modified" Clausius-Mossotti relation:[36]

$$\varepsilon = \left(\frac{8\pi\alpha_{iso}}{3V_M} + 1\right)\Big/\left(1 - \frac{4\pi\alpha_{iso}}{3V_M}\right), \quad (11)$$

where V_M is the molecular volume.

The structural differences among the various excited states were quantified in terms of the RMSDs considering only the heavy (i.e. non-hydrogen) atoms using the VMD software.[37]

3. Results and Discussion

a. Molecular Structures of PCB-asa and PCB^p in the Ground State. Panels (d), (e), and (f) in Figure 1 show the optimized structures of PCB^{p}1, PCB^{p}2, and PCB^{p}3, respectively. These optimized geometries are those obtained in the ground state for the ε = 4 environment. The resulting backbone structures of the four pyrrole rings are very close to each other for all the PCB^{p}s. Noticeable differences were found for the conformations of the two propionic acid groups in the B and C rings and the ethyl group in the A ring. These conformational differences in the side chains are responsible for variations in the physical properties of each PCB^p.

b. Absorption Spectra of PCB^p in the ε = 4 Environment. Figure 2 shows the calculated absorption spectra of PCB^{p}1, PCB^{p}2, and PCB^{p}3 in the ε = 4 environment. The overall absorption spectrum (purple line) of C-PC was obtained by summing the contributions of the three PCB^{p}s (PCB^{p}1 + PCB^{p}2 + PCB^{p}3). The experimental peaks corresponding to the Q band range between 450 and 700 nm and are reported in Table 1. The experimental results for the C-PC were obtained under a 5 mM potassium phosphate (pH 7.0) condition.[7] The experimental absorption peaks at the Q band are 618, 624, 594 nm for PCB^{p}1, PCB^{p}2, and PCB^{p}3, respectively.[7] Our computational results are located at 578.43, 592.8, and 567.53 nm, respectively, thus affected by an underestimation resulting in a constant shift of 30 to 40 nm. Nonetheless, the order of the peaks, the gross feature and the qualitative trend are in agreement with the experimental outcome. Coming to the Soret band, we rmark that this band is found in the range between 350 and 450 nm, thus still in agreement with the experiments. From these results, we can infer that the main electronic

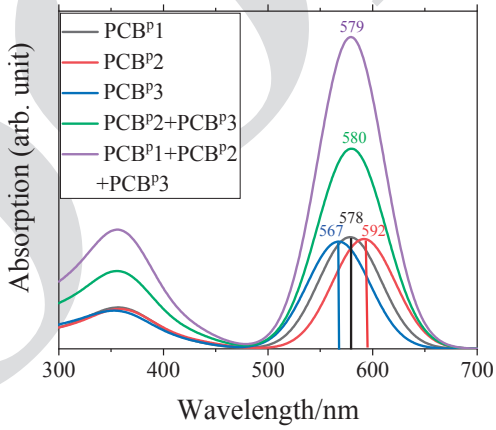


Figure 2. Calculated absorption spectra of PCB^{p}1 (black), PCB^{p}2 (red), and PCB^{p}3 (blue) in the ε = 4 environment. The green line shows the β–subunit spectrum (PCB^{p}2 + PCB^{p}3) and the purple line the whole C-PC (PCB^{p}1 + PCB^{p}2 + PCB^{p}3).

Table 1. Maximum wavelengths (λ_{max}/nm) for PCB^{p}1, PCB^{p}2, and PCB^{p}3 in different solvents. The shorthand notations for the solvents are as indicated in the caption of Figure 3.

Solvents	PCB^{p}1	PCB^{p}2	PCB^{p}3
Gas	551.85	563.39	543.53
ε = 4	578.43	591.67	567.53
ACN	578.38	591.48	568.09
CT	589.49	603.43	577.42
CF	586.80	600.54	575.26
Cy	587.62	601.43	575.69
DMSO	583.58	596.99	572.90
EtOH	579.71	592.91	569.27
n-Hp	585.10	598.75	573.39
MeOH	577.21	590.24	567.01
ε = 78.39	577.46	590.49	567.31
Exp.[6]	618	625	594

© 2021 The Chemical Society of Japan

transition occurs from the HOMO to the LUMO. The Q band is assigned to the π-π* transition.[10–17]

The absorption spectrum of the β–subunit of C-PC was calculated as a sum of the two separated contributions of PCB^{p}2 and PCB^{p}3 (PCB^{p}2 + PCB^{p}3, green line in Figure 2). Mimuro and coworkers reported that the absorption spectrum of the β–subunit has a slightly wider peak width than that of α-subunit in C-PC.[7] Consistent with this experimental result, our calculated spectral width of PCB^{p}2 + PCB^{p}3 (76.95 nm) is slightly wider than that of the PCB^{p}1 (70.64 nm). The reasons for this broadening, termed "nonhomogeneous broadening" in the literaure, have been analyzed by Ren and coworkers.[11] The calculated peak widths for the β–subunit of C-PC (PCB^{p}2 + PCB^{p}3) and for the overall C-PC (PCB^{p}1 + PCB^{p}2 + PCB^{p}3) are 76.95 nm and 75.35 nm, respectively. According to our analysis, the slight broadening originates from the fact that the spectral peak top of PCB^{p}1 lies in the middle of those of PCB^{p}2 and PCB^{p}3 so that the absorption of PCB^{p}1 does not apparently contribute to the spectral width broadening.

We note that the shoulder peak observed around 565–570 nm for the C-PC is not accurately reproduced in Figure 2.[7] The reason can be attributed to the excluded amino acid residue of Asp-87 in the model system.[10,11]

In Supporing Information, we compared the absorption spectra with and without the nearby aspartate residues, Asp87, Asp87, and Asp39, for the PCB-asa1 and PCB^{p}1, PCB-asa2 and PCB^{p}2, and PCB-asa3 and PCB^{p}3, respectively, which are covalently bound via the cystein residues of α-84, β-84, and β-155, respectively. From the comparisons, we further investigated the competitive influence of the aspartate residue and two propionic acids on the absorption spectra. The most important conclusion is that the adjacent two propionic acids rather than the aspartate residues play a key role in realizing the different photo-response among the three isomers, PCB-asa1, PCB-asa2, PCB-asa3, or PCB^{p}1, PCB^{p}2, and PCB^{p}3.

c. Comparison of the Absorption Spectra of PCB^{p} in Different Solvent Environments. The changes that the simulated adsorption spectra undergo according to the environment are summarized in Figure 3, in which panel (a) refers to PCB^{p}1, panel (b) to PCB^{p}2, and panel (c) to PCB^{p}3. We note that the absorption spectra in the gas phase undergo a significant hypochromic shift, accompanied by a decrease of the peak intensities with respect to the corresponding solvation environments for all the three chromophores. This trend is similar to those found in former studies.[14] We remark that all the geometries of Figure 3 are optimized in the $\varepsilon = 4$ environment. Hence, we can infer that neither the environment nor the molecular geometry are responsible for the features observed in the absorption spectra. Contrary to the gas phase, in the liquid environment, the shapes and the peak positions of the absorption spectra display only slight changes depending on the type of solvent. This implies that the absorption of the chromophores is mainly determined by the intrinsic chromophore properties, rather than the surrounding environment. This seems to be in accord with the finding that the exact nature of the hydrogen bonding exerted on the quinone does not matter if the surrounding environment is polar. This translates into the fact that the dielectric constant of the environment has to be high to obtain the correct electron affinity of the quinone.[32]

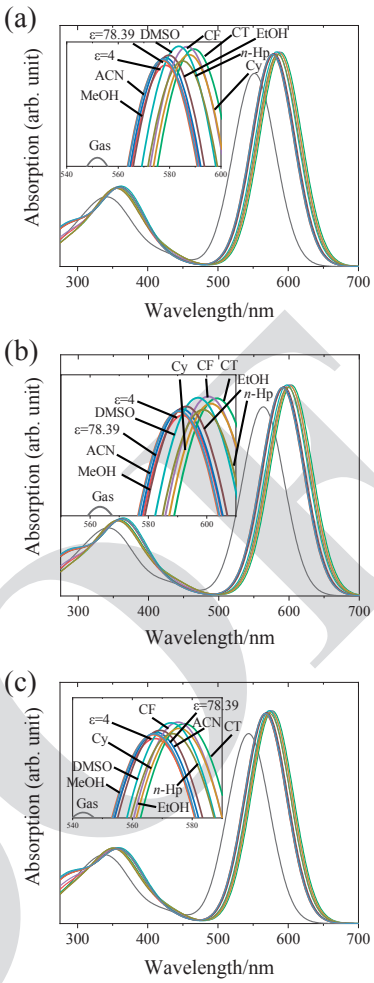


Figure 3. Calculated absorption spectra of (a) PCB^{p}1, (b) PCB^{p}2, and (c) PCB^{p}3 in diffrent solvents. The molecular geometries are optimized in the $\varepsilon = 4$ environment for all the absorption spectra. The solvents considered here are the gas phase (Gas), $\varepsilon = 4$ ($\varepsilon = 4$), acetonitrile (CH_3CN (ACN)), carbon tetrachloride (CCl_4 (CT)), chloroform ($CHCl_3$ (CF)), cyclohexane (C_6H_{12} (Cy)), dimethylsulfoxide ($(CH_3)_2SO$, (DMSO)), ethanol (CH_3CH_2OH (EtOH)), *n*-heptane (*n*-$CH_3(CH_2)_5CH_3$ (*n*-Hp)), methanol (CH_3OH (MeOH)), and water (H_2O ($\varepsilon = 78.39$)). The inset shows the details of the first absorption peaks.

In Table 1, we report the longest and shortest absorption wavelengths of PCB^{p}2 and PCB^{p}3 for all the solvent environments, in line with the results of Ren and coworkers.[11] The absorption peak tops can be shifted by 30 nm as the solvent dielectric constant (ε) increases.

d. Natural Bond Orbital (NBO) Analysis. Molecular orbitals are versatile tools to investigate chemical bonding and reactivities. Specifically, frontier orbitals, namely the HOMO and LUMO, play a pivotal role in determining the molecular characteristics. Most chemical reactions involve a redistribution of electrons leading to the formation and cleavage of chemical bonds, along with electron transfers resulting in oxidation or reduction of the system.

The textbook definition of HOMO is the molecular orbital having the highest energy among all the occupied orbitals in

© 2021 The Chemical Society of Japan

Table 2. Chemical characters of PCB^{p}1, PCB^{p}2, and PCB^{p}3 in the $\varepsilon = 4$ environment.

chromophore	PCB^{p}1	PCB^{p}2	PCB^{p}3
E_{HOMO}/eV	−6.102	−6.138	−6.111
E_{LUMO}/eV	−3.850	−3.953	−3.791
E_{GAP}/eV	2.252	2.185	2.320
IP/eV	6.102	6.138	6.111
EA/eV	3.850	3.953	3.791
χ/eV	4.976	5.045	4.951
η/eV	1.126	1.093	1.160
S/eV^{-1}	0.888	0.915	0.862
μ/Debye	4.147	5.733	3.523
α_{iso}/bohr^3	748.764	762.245	726.070
α_{aniso}/bohr^3	914.903	957.155	852.150
V_M/bohr^3	5526.842	4606.032	5439.296
ε	4.94	7.78	4.80

the ground state. As such, the HOMO is the orbital from which the removal of one electron is the energetically less demanding. For this reason, the HOMO is regarded as a Lewis-base electron donor from which electrons can be transferred to other bonds or chemical species. On the other hand, the LUMO, the molecular orbital having the lowest energy among all the unoccupied states in the ground state, is the one that is energetically more accessible, thus playing the role of an electron acceptor. Thus, the LUMO acts as a Lewis-acid electron acceptor. In this picture, a small HOMO-LUMO gap becomes an indicator of high chemical reactivity, large polarizability, low kinetic stability, and soft nature of the molecule.[38,39]

The reactive parameters for PCB^{p}1, PCB^{p}2, and PCB^{p}3 in the $\varepsilon = 4$ environment are summarized in Table 2. In general, the HOMO-LUMO gap, E_{GAP}, is relatively small (~2.2 eV), corresponding to the long-wavelength absorption maxima shown in Figures 2 and 3. Because of the small value of E_{GAP}, the hardnesses, η, are correspondingly small, as can be seen from eqs (4) and (6). Accordingly, the global softnesses, S, are very large. In particular, PCB^{p}2 has the smallest E_{GAP}, the highest absolute electronegativity χ, the smallest hardnesses η, and the largest global softness S. This indicates that PCB^{p}2 is the most reactive.

As mentioned, PCB^{p}2 has the smallest HOMO-LUMO gap, with a value corresponding to the longest absorption wavelength for the main absorption peak (see Table 1 and Table 2 in the work by Ren and coworkers[11]). The dielectric constants, ε, are the highest for PCB^{p}2 in comparison with PCB^{p}1 and PCB^{p}3 in the $\varepsilon = 4$ environment. In general, the dielectric constant increases as the isotropic polarizability, α_{iso}, becomes higher and the molecular volume, V_M, decreases, as can be deduced from eq (11). Analogously, from Table 2, we remark that the isotropic polarizability is the highest and the molecular volume is the lowest for PCB^{p}2 in the $\varepsilon = 4$ environment. Not only the dielectric constant, but also the dipole moment is the highest for PCB^{p}2 (see Figure S6 in the SI). This NBO comprehensive analysis suggests that PCB^{p}2 is likely to be the chromophore having the strongest interaction with the surrounding environment; the MEP map analyses (Figure S4 in the SI) corroborates this conclusion. Ren and coworkers[11] pointed out that the Förster energy transfer proceeds between PCB^{p}3 (β-155) and PCB^{p}2 (β-84), where the light is absorbed

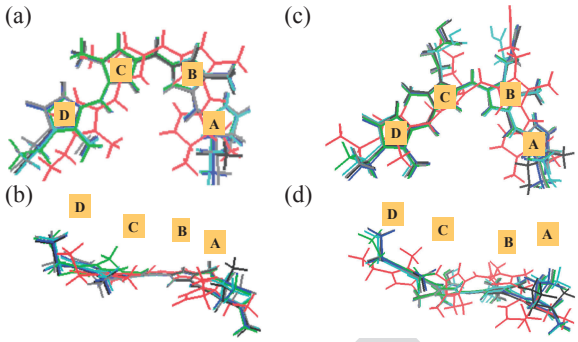


Figure 4. Superimposed optimized structures of PCB-asa1 (panels (a) and (b)) and PCB^{p}1 (panels (c) and (d)) in the ground and excited states for the $\varepsilon = 4$ environment. Panels (a) and (c) present a front view of the structure, and panels (c) and (d) a side view. The molecular structures are colored in gray for the ground state, blue for the first excited state, red for the second, green for the third, black for the fourth, and cyan for the fifth. The molecular orientations in panels (a) and (c) are identical to Figure 1.

by the former and subsequently transferred to the latter, and then the energy is transferred to PCB^{p}2. The NBO characteristics of PCB^{p}2 indicate that PCB^{p}2 can act as an efficient fluorescent moiety chromophore in the energy transfer between PCB^{p}2 and PCB^{p}3.[11]

e. Structural Changes of PCB-asa1 and PCB^{p}1 in the Excited States. To show the modifications the molecular structures of PCB-asa1 and PCB^{p}1, in the $\varepsilon = 4$ environment, undergo upon excitation, the optimized structures up to the 5th excited states are superimposed in Figure 4. We can see that the geometrical changes in the first excited state with a large absorption in the Q band ($\lambda = 578.43$ nm), are small. Conversely, in the higher excited states, as the 2nd excited state in the $\varepsilon = 4$ environment ($\lambda = 420.58$ nm for PCB-asa1 and $\lambda = 419.03$ nm for PCB^{p}1), large structural changes can be observed. It is worthy of note to stress the fact that the presence or absence of two adjacent propionic acid groups leads to significant differences in the optimized structures of the excited states. It can be noted that the excited states of PCB^{p}1 possesses a wide variety of configurations in comparison with PCB-asa1.

The structural changes of the excited states compared to the ground state were quantified in terms of the RMSD and reported in Table 3 for PCB-asa1 and PCB^{p}1 and in the $\varepsilon = 4$ environment (Figure S7 shows a two-dimensional graphical version). The RMSD of each state strongly depends on the presence or absence of two adjacent propionic acid groups. For instance, the RMSD values of the 1st and 2nd excited states increase monotonically as the degree of excitation increases (2.3250 Å for PCB-asa1 and 1.7604 for PCB^{p}1, respectively), while those of the other excited states do not show such a simple tendency. The RMSDs are small for the 3rd, 4th, and 5th excited states of PCB-asa1 (0.6250, 0.4301, and 0.2977 Å, respectively). On the other hand, the 3rd and 4th excited states have RMSDs (1.8039 and 1.7125 Å, respectively) close to the 2nd excited state (1.7604 Å). Finally, the RMSD of PCB^{p}1 is very small for the 5th excited state (0.1600 Å).

The RMSDs of the first excited state of both PCB-asa1 (0.2433 Å) and PCB^{p}1 (0.1755 Å) are small, suggesting that the

© 2021 The Chemical Society of Japan

Table 3. RMSDs and energies of the excited states relative to the ground state of PCB-asa1 and PCB^{p}1 in the $\varepsilon = 4$ environment. The two-dimensional plot for the RMSDs is shown in Figure S7.

Exited state	RMSD/Å for PCB-asa1 (λ/nm)	RMSD/Å for PCB^{p}1 (λ/nm)
1st	0.2433 (583.93)	0.1755 (578.43)
2nd	2.3250 (420.58)	1.7604 (419.03)
3rd	0.6250 (386.60)	1.8039 (379.06)
4th	0.4301 (375.41)	1.7125 (369.26)
5th	0.2977 (358.62)	0.1600 (362.84)

structural changes in PCB^{p} upon photoexcitation for the Q band region is limited, and the energy loss upon the photoexcitation and the energy transfer are minimal for PCB^{p}. As the Q band is a HOMO-LUMO transition,[10,11,13,17] the excitation still maintains the planarity of the π-conjugated pyrrole rings in the ground state.

Instead, in the 2nd excited states, large structural changes amounting to 2.3250 Å for PCB-asa1 and 1.7604 Å for PCB^{p}1 were observed. Among the excited states of PCB-asa1, the structural change in the 2nd excited state is the largest, and the excitation energy of $\lambda = 282.93$ nm lies in the Soret band region. Higher excited states up to the fifth state show structures closer to the ground and first excited states of PCB-asa1 as shown in panels (a) and (b) of Figure 4. Among the results obtained for PCB^{p}1, structural changes in the 2nd (419.03 nm), 3rd (379.06 nm), and 4th (369.26 nm) excited states, all belonging to the Soret band region, are large. Structures in the 2nd and 3rd excited states are similar, while that in the 4th excited state presents remarkable variations compared to the ground and the 2nd excited states of PCB^{p}1. These structural changes can be better analyzed by local structural parameters, namely bond lengths, angles, and dihedrals.

These quantitative investigations provide additional support to the conclusions drawn from a simple inspection of the molecular structures of Figure 4. The RMSDs for the 2nd excited state of PCB-asa1 (2.3250 Å) and for the 2nd and 3rd excited states of PCB^{p}1 (1.7604 and 1.8039 Å, respectively), where the torsion of the pyrrole ring A occurs, are large. So far, it is still unclear why the RMSD of the 4th excited state (1.7125 Å) is comparable to those of 2nd and 3rd excited states (1.7604 and 1.8039 Å, respectively) for PCB^{p}1.

Note in passing that the absorption wavelengths are nearly identical both for PCB-asa1 and for PCB^{p}1. This is due to the fact that the HOMO and LUMO electronic orbitals are centered and spread over the conjugated four pyrrole rings, A, B, C, and D, in both PCB-asa1 and PCB^{p}1, but not on two adjacent propionic acid groups (See Figures S9 and S10). Therefore, the presence of the propionic acid side chains does not play any role in the photoabsorption processes.

To get a better insight into the geometrical features of PCB-asa1 and PCB^{p}1, we compared the bond lengths, $d_{i,i+1}$, interatomic angles $\theta_{i-1,i,i+1}$, and backbone dihedral angles, $\varphi_{i,i+1,i+2,i+3}$, in the ground and the excited states from the first to the fifth for each model; here, the index i indicates the labels of the C atoms in the pyrrole rings (see Figure 5). The detailed numerical values are reported in Tables S5–S10. Hereafter, we

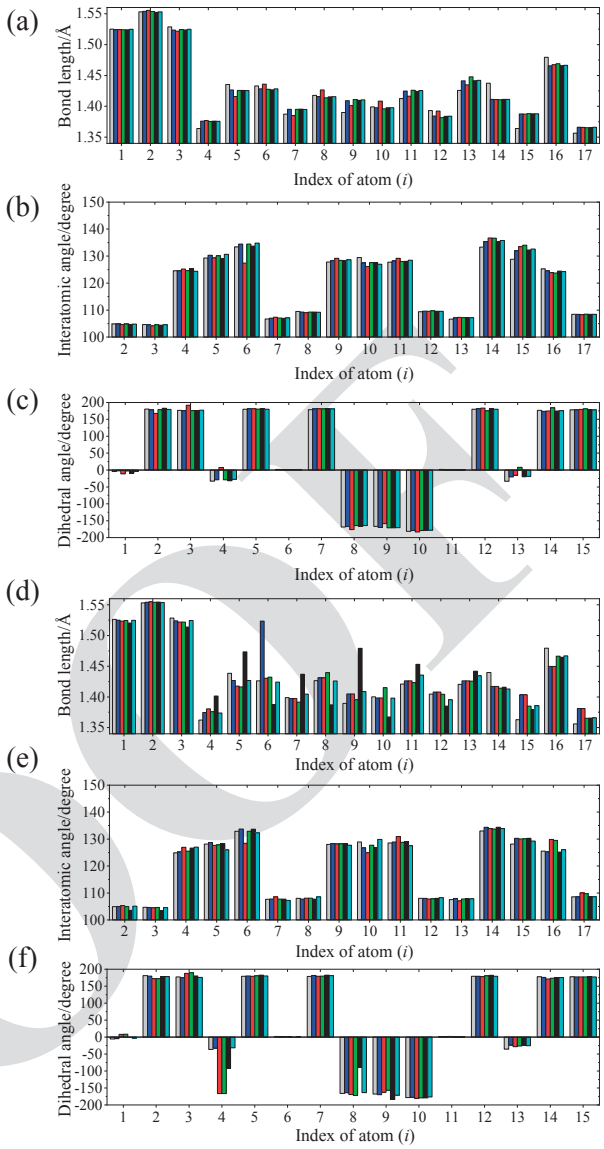


Figure 5. Bond lengths, $d_{i,i+1}$, ((a) and (d)), angles, $\theta_{i-1,i,i+1}$, ((b) and (e)), and dihedral angles, $\varphi_{i,i+1,i+2,i+3}$, ((c) and (f)) in the ground and the excited states from the first to the fifth for the PCB-asa1 and PCB^{p}1. The gray, blue, red, green, black, and light blue bars correspond to the ground, 1st, 2nd, 3rd, 4th, and 5th excited states, respectively.

indicate the numerical values parenthesis for the ground and the 1st, 2nd, 3rd, 4th, and 5th excited states, respectively. Each time that a noticeable change occurs, we evidence the corresponding value in bold font for the sake of clarity.

Starting with a comparison of the bond lengths of the respective states for PCB-asa1 and PCB^{p}1, from panel (a) of Figure 5, we can read $d_{1,2}$ (1.526, 1.525, 1.523, 1.525, 1.520, and 1.525 Å), $d_{2,3}$ (1.553, 1.554, 1.555, 1.554, 1.555, and 1.554 Å, and $d_{3,4}$ (1.529, 1.524, 1.522, 1.522, 1.514, and 1.524 Å). These are significantly larger than any other bond length, and the reason is that these consist of C-C single bonds, as seen in Figure 1(a). On the contrary, $d_{4,5}$ (1.362, 1.375, 1.381, 1.376, 1.401, and 1.374 Å) and $d_{17,18}$ (1.356, 1.381,

© 2021 The Chemical Society of Japan

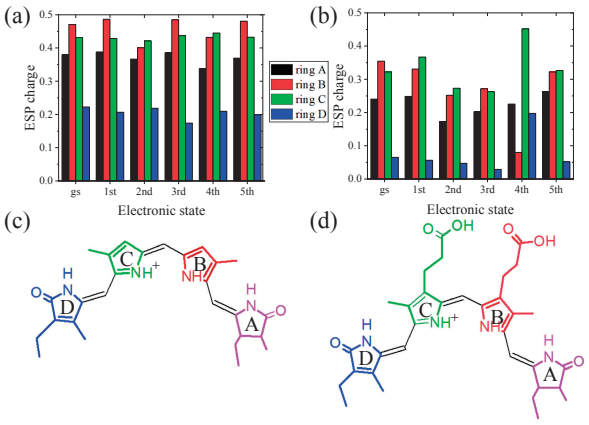


Figure 6. ESP charge distributions for the pyrrole rings in (a) PCB-asa1 and (b) PCB^{p}1 in the ground and excited states. The ESP charges were calculated by selecting the atoms colored in purple (for ring A), red (for ring B), green (for ring C), and blue (for ring D) for PCB-asa1 (panel (c)) and for PCB^{p}1 (panel (d)).

1.381, 1.365, 1.365, and 1.366 Å) are considerably shorter than any other bond length. This can be explained by the fact that these bonds are C=C double bonds. Moreover, $d_{9,10}$ (1.390, 1.405, 1.405, 1.395, 1.479, and 1.409 Å) and $d_{10,11}$ (1.400, 1.398, 1.398, 1.415, 1.367, and 1.398 Å) are very close and nearly insensitive to the excitation state. The trend shown for PCB-asa1 holds also for PCB^{p}1 as shown in panel (d).

The observed bond lengths trend is in agreement with the one reported by Durbeej.[14] He rationalized this trend in terms of the resonance structures, **II** and **III**, shown in Figure S8, which provide the major contribution among all the possible resonance structures, **I**, **II**, **III**, and **IV** (see Figure S8). The resonance structures, **II** and **III**, are dominant for all the states, independent of the presence or absence of two adjacent propionic acid groups. This is also confirmed in Figure 6, showing that the pyrrole rings B and C carry an excess of positive charge in comparison with the pyrrole rings A and D for all the states and for both PCB-asa1 and PCB^{p}1.

We can also observe that the bond lengths of PCB-asa1 are almost identical for all the states, as shown in panel (a), whereas several bond lengths of PCB^{p}1 show more or less pronounced changes depending on the state (see panel (d)). Remarkable changes can bee seen in (panel (d)): $d_{6,7}$ in the 1st excited state (1.426, 1.523, 1.430, 1.432, 1.387, and 1.424 Å), and $d_{5,6}$ (1.439, 1.427, 1.418, 1.416, 1.473, and 1.427 Å), $d_{9,10}$ (1.390, 1.405, 1.405, 1.395, 1.479, and 1.409 Å), $d_{11,12}$ (1.421, 1.426, 1.426, 1.423, 1.453, and 1.436), and $d_{13,14}$ (1.421, 1.426, 1.426, 1.426, 1.442, and 1.435 Å) in the 4th excited state of PCB^{p}1. Panel (a) of Figure 7 shows that the pyrrole ring C is more positively charged than any other ring and any other state for the 4th excited state for PCB^{p}1. These facts indicate that the 4th excited state for PCB^{p}1 is a peculiar one in which the resonance structure **III** of Figure S8 is particularly dominant for PCB^{p}1 whereas both resonance structures, **II** and **III**, in Figure S8 contribute to the molecular charge distributions in the other states.

Panels (b) and (e) in Figure 5 show that the interatomic angles are affected neither by the electronic excitations nor the

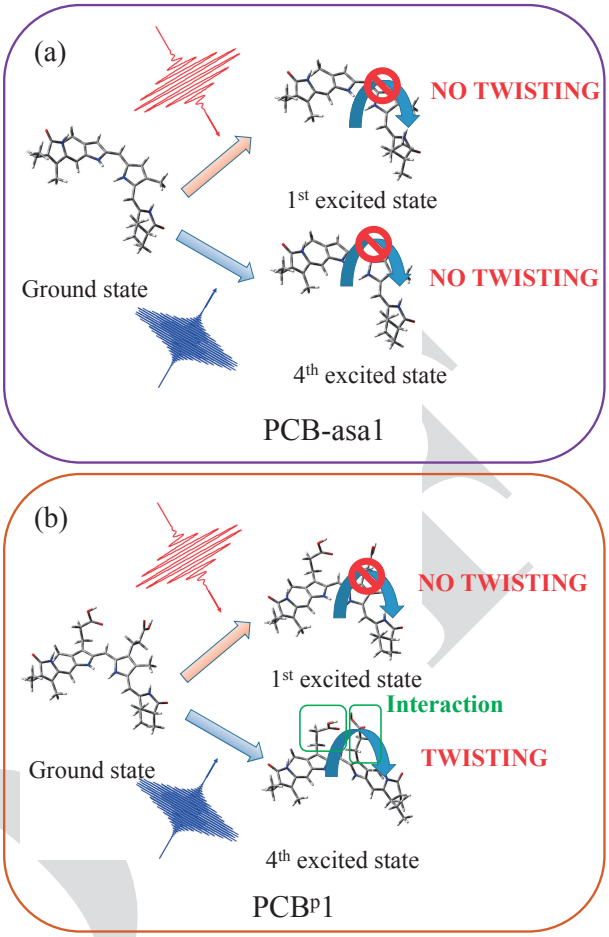


Figure 7. Schematic illustration of the interaction of two adjacent propionic acid groups. In the case of PCB-asa1 (a), the absence of two adjacent propionic acid groups does not lead to the twisting of the backbone of the pyrrole rings. On the other hand, the interaction of the two adjacent propionic acid groups leads to a twisting of the backbone pyrrole rings for the 4th excited state of PCB^{p}1 (b), which makes PCB^{p}1 peculiar in the photoabsorption mechanism.

presence or absence of two adjacent propionic acid groups. Furthermore, the interatomic angles are symmetric with respect to the C10 atom, and this reflects the symmetry of the molecular backbone with respect to C10 (panels (a) and (e) of Figure 1).

Panels (c) and (f) in Figure 5 show the backbone dihedral angles. The dihedral angles that represent the planarity of the pyrrole rings and π-conjugation are $\varphi_{1,2,3,4}$ (−4.40, −2.39, −11.59, −2.90, −9.38, and −4.03 deg. for PCB-asa1, while −5.67, −4.72, 8.03, 8.67, 0.24, and −3.11 deg. for PCB^{p}1), $\varphi_{6,7,8,9}$ (1.99, 1.20, 1.07, 1.27, 1.40, and 1.43 deg. for PCB-asa1, while 1.90, 1.16, 1.32, 1.06, 0.14, and 1.13 deg. for PCB^{p}1), and $\varphi_{11,12,13,14}$ (1.87, 0.83, 1.07, 0.89, 0.62, and 0.92 deg. for PCB-asa1, while 1.58, 1.08, 1.81, 1.11, 0.45, and 1.02 deg. for PCB^{p}1). A significant change of the dihedral angles as a function of the electronic excitation is detected for $\varphi_{4,5,6,7}$ (−32.60, −29.08, 7.59, −28.91, −31.93, and −27.64 degs. for PCB-asa1, while −36.08, −32.32, −166.56, −166.46, −91.60, and −31.52 deg. for PCB^{p}1), corresponding to a torsion between the pyrrole rings A and B around the C5-C6 bond.

© 2021 The Chemical Society of Japan

These values indicate that there are remarkable torsional rotations around the 5–6 bond for the 2nd excited state for PCB-asa1 and for the 2nd, 3rd, and 4th excited states of PCB^{p}1.

These changes account for two torsional rotations. One corresponds to a complete torsion of pyrrole ring A around the C5-C6 bond with the dihedral angles being $\varphi_{4,5,6,7} = 7.59$ deg. for the 2nd excited state of PCB-asa1 and $\varphi_{4,5,6,7} = -166.56$ and -166.46 deg. for the 2nd and 3rd excited states of PCB^{p}1, respectively. The second one corresponds to an incomplete torsion of the pyrrole ring A around the C5-C6 bond, with the dihedral angles being $\varphi_{4,5,6,7} = -91.60$ deg. for the 4th excited state of PCB^{p}1.

On the other hand, the dihedral angles for $\varphi_{8,9,10,11}$ are (-165.80, -164.21, -169.37, -172.25, -88.98, and -163.63 degs.) for PCB^{p}1. If all the angles $\varphi_{8,9,10,11}$ are equal to about $-165°$, the pyrrole rings B and C are almost coplanar. Instead, the dihedral angle, $\varphi_{8,9,10,11} = -88.98$ degs. for the 4th excited state of PCB^{p}1 deviates significantly from this value, and this results in pyrrole rings B and C being orthogonal to each other upon rotation around the C9-C10 single bond. The fact that the bond order of the C9-C10 bond is one for the resonance structures **III** in Figure S8, but that it is not for the resonance structure **II** in Figure S8 is actually in accord with the finding that the 4th excited state for PCB^{p}1 can easily undergo the mentioned torsional rotation around the C9-C10 bond.

The HOMO and LUMO orbitals in the molecular configuration optimized for the 4th excited state of PCB^{p}1, shown in panels (e) and (f) of Figure S10, provide additional support of our conclusions. While the HOMO is localized on the pyrrole rings A and B (panel (e)), the LUMO is localized above the pyrrole rings C and D (panel (f)). This implies that the π-conjugation of the two pyrrole rings, B and C, is broken at C10 by the vertical positions of the two pyrrole rings and a positive charge accumulation occurs on ring C.

Figure 6 shows the electrostatic potential (ESP) charge distributions[40] of PCB-asa1 and PCB^{p}1 for the pyrrole rings of Figure 1 for each state. The pyrrole rings B and C are more positively charged than A and D in both PCB-asa1 and PCB^{p}1. This is agrees with the fact that the resonance structures, **II** and **III**, shown in Figure S8, provide the major contribution among all the possible resonance structures, **I**, **II**, **III**, and **IV** (Figure S8). Interestingly, panel (b) of Figure 6 shows that the pyrrole ring C is highly positively charged for the 4th excited state of PCB^{p}1. This is consistent with the fact that the resonance structure **III** in Figure S8 dominates with respect to the other resonance structures.

Finally, Figure 7 summarizes the induced structural changes in the excited states. Panel (a) shows that in the case of PCB-asa1, the absence of two adjacent propionic acid groups makes difficult twisting of the backbone pyrrole rings in the 1st excited and 4th excited states. On the other hand, panel (b) shows that the interaction between the adjacent two propionic acid groups is not very strong for the 1st excited state so that the photo-excitation from the ground to the excited state does not induce any significant structural change of PCB^{p}1. However, the interaction is strong enough for the 4th excited state to induce a torsional motion of the backbone pyrrole rings.

These results suggest that PCB in C-PC possesses efficient photo-response properties in which the photo-induced structural changes are minimized in the Soret band region, but they are accessible in higher excited states of the Q band region. These properties are peculiar to this system in clear contrast with other photo-responsive molecules, such as *p*-coumaric acid in the photoactive yellow protein (PYP) and retinal in rhodopsin.

4. Conclusion

The present study focuses on the role played by two interacting adjacent propionic acid groups of the C-PC chromophores of PCB in the photoexcitation processes. By resorting to well assessed computational tools, TDDFT calculations were used to simulate the absorption spectra of PCB^{p}s, complemented by an NBO analysis to get a deeper insight into the chemical reaction mechanism. Separate absorption spectra analyses of the α– and β–subunits have evidenced that the spectral width broadening observed experimentally for the latter subunit was attributed to its nonhomogeneous distribution of two different absorption peaks of the PCB^{p}s in the β-subunit. The NBO analyses suggested that although the three types of PCB^{p}s have identical molecular formulae, the physical and chemical properties are significantly different. Furthermore, the structural changes of PCB^{p}1 upon electronic excitation were investigated by comparing the major geometrical parameters (RMSD, bond lengths, interatomic angles, and backbone dihedral angles) to the ground state. The propionic acid groups of PCB^{p}1 have been shown to induce a characteristic torsional motion of the backbone pyrrole rings in the 4th excited state.

In addition, the investigations on the competitive influence of the nearby aspartate residue and two propionic acids on the absorption spectra have shown that the propionic acids play a significant role in realizing the different photo-response among the three isomers of PCB, and presence of the nearby aspartate residue is almost insensitive to the peak separation of the absorption spectra (calculated absorption spectra and more detailed discussions are provided in Figures S4–S9 of the Supporting Information).

The present theoretical study has also shown that the 1st excited state of PCB^{p}s in the Soret band region induces minimal structural changes. On the other hand, the higher excited states in the Q band region are characterized by larger structural changes altering the pyrrole rings. The small structural change in the 1st excited state is favorable for an efficient and fast photoabsorption and energy transfer, needed for the light-harvesting processes of chromophores in natural photosynthesis. The large structural changes in the higher excited state also represent a protection of the system from photodamage by high-energy photons and allow release of the excess energy. Since these features are present in the PCB, the outcome of our study of the excited-state provides a novel perspective for an ideal light-harvesting chromophore not only in natural photosynthesis but also in artificial related processes. Moreover, we expect that this work can promote future research efforts in the field of chromophores, with special emphasis on spectroscopic and time-resolved X-ray structural investigations.

This research was supported by JSPS KAKENHI ground numbers 17H04866, 18H05154, 19H05781, 20H05088 and JST, PRESTO Grant Number JPMJPR19G6, Japan. Numerical

© 2021 The Chemical Society of Japan

calculations were carried out under the support of (1) Multidisciplinary Cooperative Research Program in CCS, University of Tsukuba, (2) HPCI system research project (project ID: hp19110) using the computational resource of CX400 provided by the Information Technology Center in Nagoya University. M.B. thanks the HPC Mesocentera at the University of Strasbourg funded by the Equipex Equip@Meso project (Programme Investissements d'Avenir) and the CPER Alsacalcul/Big Data, and the Grand Equipement National de Calcul Intensif (GENCI) under allocation DARI-A0080906092.

Supporting Information

The following files are available free of charge. This material is available on https://doi.org/10.1246/bcsj.20200187.

Comparison between the initial and optimized geometries of PCB^{p}1, PCB^{p}2, and PCB^{p}3 (Figure S1).

Optimized molecular structures of PCB-asa1, PCB-asa2, and PCB-asa3 with the aspartate residues (Figure S2).

Calculated absorption spectra of PCB-asa1, PCB-asa2, and PCB-asa3 in the $\varepsilon = 4$ environment (Figure S3).

Superposition of calculated absorption spectra of PCB-asa1, PCB-asa2, and PCB-asa3 in the $\varepsilon = 4$ environment (Figure S4).

Calculated absorption spectra of PCB^{p}1, PCB^{p}2, and PCB^{p}3 in the $\varepsilon = 4$ environment (Figure S5).

Calculated absorption spectra of PCB-asa1, PCB-asa2, and PCB-asa3 with the aspartate residues (Figure S6).

Superposition of calculated absorption spectra of PCB-asa1, PCB-asa2, and PCB-asa3 with the aspartate residues (Figure S7).

Calculated absorption spectra of PCB^{p}1, PCB^{p}2, and PCB^{p}3 with the aspartate residues (Figure S8).

Superposition of calculated absorption spectra of PCB^{p}1, PCB^{p}2, and PCB^{p}3 with the aspartate residues (Figure S9).

Configurations of two adjacent propionic acid chains for PCB^{p}1, PCB^{p}2, and PCB^{p}3 (Figure S10).

MEP maps of the optimized structures of protonated PCB^{p}1, PCB^{p}2, and PCB^{p}3 in the gas phase (Figure S11).

MEP maps of the optimized structures of neutral PCB^{p}1, PCB^{p}2, and PCB^{p}3 in the gas phase and in the $\varepsilon = 4$ environment (Figure S12).

Optimized molecular orbitals for PCB^{p}1, PCB^{p}2, and PCB^{p}3 (Figure S13).

Magnitudes and the directions of dipole moments of PCB^{p}1, PCB^{p}2, and PCB^{p}3 (Figure S14).

Two-dimensional plot of the RMSDs for each excited state relatve to the ground state in the $\varepsilon = 4$ environment for PCB-asa1 and PCB^{p}1 (Figure S15).

Resonance structures of PCB^{p}1 (Figure S16).

Optimized molecular orbitals for PCB-asa1 (Figure S17).

Optimized molecular orbitals for PCB^{p}1 (Figure S18).

Dipole moments of ground and excited states of PCB-asa1 and PCB^{p}1 in the $\varepsilon = 4$ environment (Figure S19).

Isotropic polarizabilities of ground and excited states of PCB-asa1 and PCB^{p}1 in the $\varepsilon = 4$ environment (Figure S20).

Anisotropic polarizabilities of ground and excited states of PCB-asa1 and PCB^{p}1 in the $\varepsilon = 4$ environment (Figure S21).

Molecular volumes of ground and excited states of PCB-asa1 and PCB^{p}1 in the $\varepsilon = 4$ environment (Figure S22).

Directions and magnitudes of dipole moments of ground and excited states of PCB-asa1 in the $\varepsilon = 4$ environment (Figure S23).

Directions and magnitudes of dipole moments of ground and excited states of PCB^{p}1 in the $\varepsilon = 4$ environment (Figure S24).

Absorption wavelengths for PCB-asa and PCB^{p} in the $\varepsilon = 4$ environment or with the aspartate residues and in the presence/absence of the propionic acids. (Table S1).

Average electron densities between H and O atoms contributing to the intramolecular hydrogen bond for PCB^{p}1, PCB^{p}2, and PCB^{p}3 (Table S2).

Ground state optimized geometries for PCB^{p}1 in the gas phase (Table S3).

Excited state optimized geometries for PCB^{p}1 in the gas phase (Table S4).

Ground state optimized geometries for PCB^{p}1 in the $\varepsilon = 4$ environment (Table S5).

Excited state optimized geometries for PCB^{p}1 in the $\varepsilon = 4$ environment (Table S6).

Bond lengths for the index of atom (*i*) shown in Figure 1 for PCB-asa1 in the $\varepsilon = 4$ environment (Table S7).

Interatomic angles for the index of atom (*i*) shown in Figure 1 for PCB-asa1 in the $\varepsilon = 4$ environment (Table S8).

Backbone dihedral angles for the index of atom (*i*) shown in Figure 1 for PCB-asa1 in the $\varepsilon = 4$ environment (Table S9).

Bond lengths for the index of atom (*i*) shown in Figure 1 for PCB^{p}1 in the $\varepsilon = 4$ environment (Table S10).

Interatomic angles for the index of atom (*i*) shown in Figure 1 for PCB^{p}1 in the $\varepsilon = 4$ environment (Table S11).

Backbone dihedral angles for the index of atom (*i*) shown in Figure 1 for PCB^{p}1 in the $\varepsilon = 4$ environment (Table S12).

Franck-Condon excited states of PCB-asa1 in the $\varepsilon = 4$ environment (Table S13).

S1 adiabatic excited states of PCB-asa1 in the $\varepsilon = 4$ environment (Table S14).

S2 adiabatic excited states of PCB-asa1 in the $\varepsilon = 4$ environment (Table S15).

S3 adiabatic excited states of PCB-asa1 in the $\varepsilon = 4$ environment (Table S16).

S4 adiabatic excited states of PCB-asa1 in the $\varepsilon = 4$ environment (Table S17).

S5 adiabatic excited states of PCB-asa1 in the $\varepsilon = 4$ environment (Table S18).

Franck-Condon excited states of PCB^{p}1 in the $\varepsilon = 4$ environment (Table S19).

S1 adiabatic excited states of PCB^{p}1 in the $\varepsilon = 4$ environment (Table S20).

S2 adiabatic excited states of PCB^{p}1 in the $\varepsilon = 4$ environment (Table S21).

S3 adiabatic excited states of PCB^{p}1 in the $\varepsilon = 4$ environment (Table S22).

S4 adiabatic excited states of PCB^{p}1 in the $\varepsilon = 4$ environment (Table S23).

S5 adiabatic excited states of PCB^{p}1 in the $\varepsilon = 4$ environment (Table S24).

References

1 A. N. Glazer, *Biochim. Biophys. Acta* **1984**, *768*, 29.

2 W. A. Sidler, Phycobilisome and phycobiliprotein struc-

© 2021 The Chemical Society of Japan

PROOF

tures, in Molecular biology of the cyanobacteria. A. D. Bryant, (Ed.), Kluwer Press, Amsterdam, The Netherlands, pp. 139–216.
3 R. MacColl, D. S. Berns, N. L. Koven, *Arch. Biochem. Biophys.* **1971**, *146*, 477.
4 R. E. Dale, F. W. Teale, *Photochem. Photobiol.* **1970**, *12*, 99.
5 A. N. Glazer, *Mol. Cell. Biochem.* **1977**, *18*, 125.
6 M. Mimuro, R. Rümbeli, P. Füglistaller, H. Zuber, *Biochim. Biophys. Acta, Bioenerg.* **1986**, *851*, 447.
7 M. Mimuro, P. Füglistaller, R. Rümbeli, H. Zuber, *Biochim. Biophys. Acta, Bioenerg.* **1986**, *848*, 155.
8 J. L. Soret, *C. R. Acad. Sci.* **1983**, *97*, 1267.
9 C. J. Weiss, *J. Mol. Spectrosc.* **1972**, *44*, 37.
10 J. Wan, X. Xu, Y. Ren, G. Yang, *J. Phys. Chem. B* **2005**, *109*, 11088.
11 Y. Ren, J. Wan, X. Xu, Q. Zhang, G. Yang, *J. Phys. Chem. B* **2006**, *110*, 18665.
12 O. A. Borg, B. Durbeej, *J. Phys. Chem. B* **2007**, *111*, 11554.
13 R. A. Matute, R. Contreras, L. González, *J. Phys. Chem. Lett.* **2010**, *1*, 796.
14 B. Durbeej, *Phys. Chem. Chem. Phys.* **2009**, *11*, 1354.
15 B. Durbeej, O. A. Borg, L. A. Eriksson, *Chem. Phys. Lett.* **2005**, *416*, 83.
16 O. Falklöf, B. Durbeej, *J. Comput. Chem.* **2013**, *34*, 1363.
17 R. A. Matute, R. Contreras, G. Pérez-Hernández, L. González, *J. Phys. Chem. B* **2008**, *112*, 16253.
18 E. Runge, E. K. Gross, *Phys. Rev. Lett.* **1984**, *52*, 997.
19 K. Pande, C. D. Hutchison, G. Groenhof, A. Aquila, J. S. Robinson, J. Tenboer, S. Basu, S. Boutet, D. P. DePonte, M. Liang, T. A. White, N. A. Zatsepin, O. Yefanov, D. Morozov, D. Oberthuer, C. Gati, G. Subramanian, D. James, Y. Zhao, J. Koralek, J. Brayshaw, C. Kupitz, C. Conrad, S. Roy-Chowdhury, J. D. Coe, M. Metz, P. L. Xavier, T. D. Grant, J. E. Koglin, G. Ketawala, R. Fromme, V. Srajer, R. Henning, J. C. Spence, A. Ourmazd, P. Schwander, U. Weierstall, M. Frank, P. Fromme, A. Barty, H. N. Chapman, K. Moffat, J. J. van Thor, M. Schmidt, *Science* **2016**, *352*, 725.
20 T. R. Barends, L. Foucar, A. Ardevol, K. Nass, A. Aquila, S. Botha, R. B. Doak, K. Falahati, E. Hartmann, M. Hilpert, M. Heinz, M. C. Hoffmann, J. Kofinger, J. E. Koglin, G. Kovacsova, M. Liang, D. Milathianaki, H. T. Lemke, J. Reinstein, C. M. Roome, R. L. Shoeman, G. J. Williams, I. Burghardt, G. Hummer, S. Boutet, I. Schlichting, *Science* **2015**, *350*, 445.
21 J. M. Glownia, J. Cryan, J. Andreasson, A. Belkacem, N. Berrah, C. I. Blaga, C. Bostedt, J. Bozek, L. F. DiMauro, L. Fang, J. Frisch, O. Gessner, M. Gühr, J. Hajdu, M. P. Hertlein, M. Hoener, G. Huang, O. Kornilov, J. P. Marangos, A. M. March, B. K. McFarland, H. Merdji, V. S. Petrovic, C. Raman, D. Ray, D. A. Reis, M. Trigo, J. L. White, W. White, R. Wilcox, L. Young, R. N. Coffee, P. H. Bucksbaum, *Opt. Express* **2010**, *18*, 17620.
22 M. Levantino, G. Schiro, H. T. Lemke, G. Cottone, J. M. Glownia, D. L. Zhu, M. Chollet, H. Ihee, A. Cupane, M. Cammarata, *Nat. Commun.* **2015**, *6*, 6772.
23 D. Arnlund, L. C. Johansson, C. Wickstrand, A. Barty, G. J. Williams, E. Malmerberg, J. Davidsson, D. Milathianaki, D. P. DePonte, R. L. Shoeman, D. Wang, D. James, G. Katona, S. Westenhoff, T. A. White, A. Aquila, S. Bari, P. Berntsen, M. Bogan, T. B. van Driel, R. B. Doak, K. S. Kjær, M. Frank, R. Fromme, I. Grotjohann, R. Henning, M. S. Hunter, R. A. Kirian, I. Kosheleva, C. Kupitz, M. Liang, A. V. Martin, M. M. Nielsen, M. Messerschmidt, M. M. Seibert, J. Sjöhamn, F. Stellato, U. Weierstall, N. A. Zatsepin, J. C. Spence, P. Fromme, I. Schlichting, S. Boutet, G. Groenhof, H. N. Chapman, R. Neutze, *Nat. Methods* **2014**, *11*, 923.
24 N. Coquelle, M. Sliwa, J. Woodhouse, G. Schirò, V. Adam, A. Aquila, T. R. M. Barends, S. Boutet, M. Byrdin, S. Carbajo, E. De la Mora, R. B. Doak, M. Feliks, F. Fieschi, L. Foucar, V. Guillon, M. Hilpert, M. S. Hunter, S. Jakobs, J. E. Koglin, G. Kovacsova, T. J. Lane, B. Lévy, M. Liang, K. Nass, J. Ridard, J. S. Robinson, C. M. Roome, C. Ruckebusch, M. Seaberg, M. Thepaut, M. Cammarata, I. Demachy, M. Field, R. L. Shoeman, D. Bourgeois, J. P. Colletier, I. Schlichting, M. Weik, *Nat. Chem.* **2018**, *10*, 31.
25 F. Weinhold, *J. Comput. Chem.* **2012**, *33*, 2363.
26 Gaussian 16, Revision C.01, M. J. Frisch, G. W. Trucks, H. B. Schlegel, G. E. Scuseria, M. A. Robb, J. R. Cheeseman, G. Scalmani, V. Barone, G. A. Petersson, H. Nakatsuji, X. Li, M. Caricato, A. V. Marenich, J. Bloino, B. G. Janesko, R. Gomperts, B. Mennucci, H. P. Hratchian, J. V. Ortiz, A. F. Izmaylov, J. L. Sonnenberg, D. Williams-Young, F. Ding, F. Lipparini, F. Egidi, J. Goings, B. Peng, A. Petrone, T. Henderson, D. Ranasinghe, V. G. Zakrzewski, J. Gao, N. Rega, G. Zheng, W. Liang, M. Hada, M. Ehara, K. Toyota, R. Fukuda, J. Hasegawa, M. Ishida, T. Nakajima, Y. Honda, O. Kitao, H. Nakai, T. Vreven, K. Throssell, J. A. Montgomery, Jr., J. E. Peralta, F. Ogliaro, M. J. Bearpark, J. J. Heyd, E. N. Brothers, K. N. Kudin, V. N. Staroverov, T. A. Keith, R. Kobayashi, J. Normand, K. Raghavachari, A. P. Rendell, J. C. Burant, S. S. Iyengar, J. Tomasi, M. Cossi, J. M. Millam, M. Klene, C. Adamo, R. Cammi, J. W. Ochterski, R. L. Martin, K. Morokuma, O. Farkas, J. B. Foresman, D. J. Fox, Gaussian, Inc., Wallingford CT, **2016**.
27 F. Furche, R. Ahlrichs, *J. Chem. Phys.* **2002**, *117*, 7433.
28 A. D. Becke, *J. Chem. Phys.* **1993**, *98*, 1372.
29 J. Nield, P. J. Rizkallah, J. Barber, N. E. Chayen, *J. Struct. Biol.* **2003**, *141*, 149.
30 GaussView, Version 6.1, R. Dennington, T. A. Keith, J. M. Millam, Semichem Inc., Shawnee Mission, KS, **201**.
31 J. Tomasi, B. Mennucci, R. Cammi, *Chem. Rev.* **2005**, *105*, 2999.
32 M. R. A. Blomberg, P. E. M. Siegbahn, G. T. Babcock, *J. Am. Chem. Soc.* **1998**, *120*, 8812.
33 T. Koopmans, *Physica (Amsterdam)* **1934**, *1*, 104.
34 A. Rauk, Orbital interaction theory of organic chemistry, 2nd Edn John Wiley & Sons: Newyork, **2001**, 34.
35 N. Adir, R. Vainer, N. Lerner, *Biochim. Biophys. Acta* **2002**, *1556*, 168.
36 S. Kraner, C. Koerner, K. Leo, E. Bittrich, K. J. Eichhorn, Y. Karpov, M. Stamm, K. Hinrichs, M. Al-Hussein, *Phys. Rev. B* **2015**, *91*, 195202.
37 W. Humphrey, A. Dalke, K. Schulten, *J. Mol. Graphics* **1996**, *14*, 33.
38 B. Kosar, C. Albayrak, *Spectrochim. Acta, Part A* **2011**, *78*, 160.
39 Y. Shyma May, N. R. El-Brollosy, A. A. El-Emam, O. A. Al-Deeb, P. J. Jojo, C. Yohannan Panicker, C. Van Alsenoy, *Spectrochim. Acta, Part A* **2014**, *133*, 449.
40 J. S. Murray, P. Politzer, *WIREs Comput. Mol. Sci.* **2011**, *1*, 153.

PROOF